A Fast and Accurate Transfer Function Validation Strategy Using Optimized Rotation-Invariant Lead Trajectories

Yu Wang , Jianfeng Zheng , *Member, IEEE*, Qingyan Wang , Ji Chen , *Senior Member, IEEE*, and Wolfgang Kainz , *Member, IEEE*

Abstract—This article demonstrates a novel strategy to effectively and efficiently validate the lead transfer function model, which is used to predict the radiofrequency induced heating near the distal end of active implantable medical devices under magnetic resonance imaging exposure. The strategy uses the particle swarm optimization (PSO) algorithm to generate optimized rotation-invariant lead trajectories for arbitrary lead lengths in a rectangular phantom. The validation trajectories are generated by rotating a PSO optimized trajectory on a circular plate. The incident electric fields along these trajectories are minimally correlated resulting in very accurate validation. Compared with other validation trajectories used in the literature and recommended by ISO/TS 10974, the new method is significantly more robust, effective, accurate, and time efficient; and therefore, an ideal candidate for standardization.

Index Terms—Active implantable metallic device (AIMD), magnetic resonance imaging (MRI), particle swarm optimization (PSO), rotational invariant lead trajectories, transfer function (TF).

I. INTRODUCTION

AGNETIC resonance imaging (MRI) examination has become a common procedure to diagnose disease nowadays. There are increasing demands for patients with an active implantable medical device (AIMD) to undergo MRI procedures. Since these devices often have a long and insulated lead body, the radiofrequency (RF) induced energy generated by the MRI RF coil can only be deposited into the human tissue at the lead-tip electrodes. Consequently, the concentrated energy deposition near the lead-tip electrode can lead to localized temperature rise and cause tissue damage [1]–[6].

To understand the mechanism of RF-induced heating, both numerical simulations and rigorously designed experiments

Manuscript received September 7, 2020; revised October 27, 2020; accepted November 16, 2020. (Corresponding author: Ji Chen.)

Yu Wang, Jianfeng Zheng, Qingyan Wang, and Ji Chen are with the Department of Electrical and Computer Engineering, University of Houston, Houston, TX 77004 USA (e-mail: ywang129@uh.edu; jzheng4@central.uh.edu; qwang25@uh.edu; jchen23@central.uh.edu).

Wolfgang Kainz is with the Center for Devices and Radiological Health, U.S. Food and Drug Administration, Silver Spring, MD 20993 USA (e-mail: wolfgang.kainz@fda.hhs.gov).

Color versions of one or more figures in this article are available at https://doi.org/10.1109/TEMC.2020.3039488.

Digital Object Identifier 10.1109/TEMC.2020.3039488

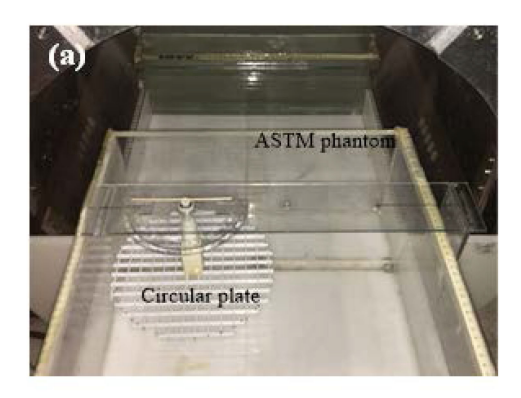
were performed by different groups [7]–[12]. Because the direct modeling of an AIMD with submillimeter lead features in a large heterogeneous media is difficult to perform, the transfer function (TF) concept was proposed to estimate the RF-induced heating near the distal end of AIMD leads [13]. Feng *et al.* [14] proposed a technique to physically measure the TF of the AIMD lead based on the equivalent principle and reciprocity theorem. Combined with the incident electric (E) field, the TF method has been utilized to predict the RF-induced heating in the vicinity of the distal end of the AIMD lead.

The ISO/TS 10974:2018 Standard prescribes that an electromagnetic model of the AIMD lead, i.e., the TF, for predicting the power deposition in the homogeneous media or tissue, shall be used and validated using a set of tangential E-field exposures [15]. Comparing measured with the computational results is referred to as the validation of a TF model. If the difference between the TF estimated and the measured temperature rise is less than the combined uncertainty, the TF model can be considered validated. Other quantities can also be used to validate the TF, e.g., the current, the temperature rises, etc. [16].

The generation of different incident E-field exposures can be achieved by placing the AIMD leads along different trajectories inside a rectangular phantom or by varying the phase and amplitude of the input power sources. We refer to the first approach as "trajectory diversity" and the second approach as "transmitter diversity" [15]–[19]. Ideally, the incident E fields of these exposures should be orthogonal to each other and generate a relatively high (two to three times higher than the background heating) lead-tip heating [20], [21]. Ideally, these validation E fields should be linearly independent, or, at least, have a low correlation. For the transmitter diversity, one would require at least ½ N independent transmitters to perform N validations.

The ISO/TS 10974 Standard suggests in Annex M [15] lead trajectories, including changes in magnitude, phase, or combinations of both. However, these trajectories are laborious because rectangular, elliptical, and circular phantoms are needed. Moreover, for short leads the incident E-field along these validation trajectories could be significantly correlated, leading to incomplete and inaccurate validation results. Feng *et al.* [14] proposes nine validation trajectories, including straight, *L*-shaped, and *U*-shaped trajectories (later referred to as SLU trajectories) inside a rectangular phantom. These trajectories have several shortcomings, as follows.

0018-9375 © 2020 IEEE. Personal use is permitted, but republication/redistribution requires IEEE permission. See https://www.ieee.org/publications/rights/index.html for more information.



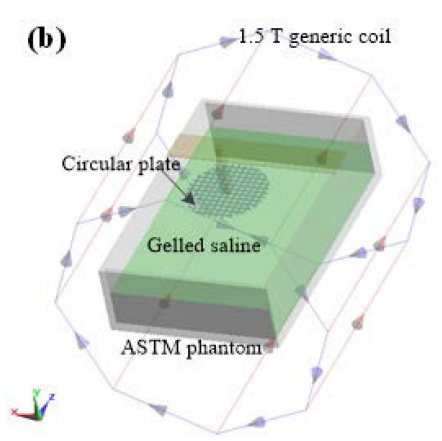


Fig. 1. (a) Rotatable circular plate with a radius $R_P = 10$ cm in the rectangular phantom to position the AIMD leads. (b) Three-dimensional computer aided design (CAD) model of the circular plate within a 1.5 T generic RF coil.

- 1) The E fields along the trajectories are highly correlated [14].
- 2) Multiple manual fixations of the lead in different phantoms result in a high uncertainty [22].
- The entire procedure is very time consuming if repeated measurements are required.

In this article, a novel method is proposed to overcome these inadequacies. Using the partial swarm optimization (PSO), we are able to design optimized validation trajectories for AIMDs with different lead lengths. These optimized trajectories minimize the correlation of the incident E-field. Using a fixed trajectory on a rotatable circular plate, which is placed inside a rectangular phantom [see Fig. 1(a)], one does not need to reposition the lead between different heating measurements. This method reduces the experimental time and eliminates the uncertainty of the temperature probe positioning. As the circular plate rotates, the lead is exposed to different incident E fields. The correlation between these incident E fields can be minimized by optimizing the fixed trajectory. Incident E fields with a low correlation reduce the measurement uncertainty and are a requirement for credible TF validation [21]. To achieve a high signal-to-noise ratio (SNR), the circular plate is positioned in the upper left corner of the rectangular phantom, where the E-field is stronger than that in the center region. This article is an expanded version of the authors IEEE APS2019 abstract [23].

The rest of this article is organized as follows. In Section II, the basic TF theory and a detailed description of the PSO algorithm to generate the optimized validation trajectories are presented. In Section III, we perform the numerical incident E-field simulations in a rectangular phantom with the rotatable circular plate. Then the PSO optimized trajectories for different lead lengths are developed and compared with nine SLU trajectories and nine trajectories based on those suggested in ISO/TS 10974. Finally, Section IV concludes this article.

II. METHODOLOGY

A. TF Method

The TF is used to estimate the RF-induced lead-tip temperature rise when the AIMD is exposed to an MRI RF coil. The lead-tip temperature rise has a close relation with the induced E-field near the lead tip. In [14], the equivalent principle and reciprocity theorem is applied to compute the induced E-field at the lead tip $\vec{E}_{\rm tip}$ as

$$\left| \vec{E}_{\text{tip}} \right| = -\int_{L} \frac{\vec{I}(l) \cdot \vec{E}_{\text{inc}}(l) \ dl}{|I_{\text{tip}}| \ \Delta l_{\text{I}}}$$
 (1)

where $\vec{E}_{\rm inc}$ is the incident E-field along the lead trajectory, which can be extracted from the E-field distribution in a phantom or human body model excited by the MRI RF coil without the lead present. \vec{I} is the current distribution on the lead, when applying the RF current source $I_{\rm tip}$ at the lead tip. L is the lead length and $\Delta l_{\rm I}$ is the length of the current source. The net temperature rise ΔT in the vicinity of the lead tip is proportional to the net specific absorption rate ${\rm SAR}_{\rm net} = \sigma E^2/\rho$ as

$$\Delta T \sim SAR_{net} = \frac{\sigma \left| \vec{E}_{\text{tip}} \right|^{2}}{2\rho} = \frac{\sigma}{2\rho} \left| \int_{L} \frac{\vec{I}(l) \cdot \vec{E}_{\text{inc}}(l) \ dl}{|I_{\text{tip}}| \ \Delta l_{\text{I}}} \right|^{2}$$
$$= A \left| \int_{L} \text{TF}(l) E_{\text{tan}}(l) \ dl \right|^{2}$$
(2)

where $E_{\rm tan}$ is the tangential component of the incident E-field; ${\rm TF}(l)$ is the TF, which is proportional to the induced current \vec{I} on the lead; A is the calibration factor; ρ and σ are the density and conductivity of the media, respectively. The TF can be derived by measuring the lead current [14]. The measurement uncertainties lead to errors in the TF. Therefore, ISO/TS 10974 requires the TF to be validated by a set of tangential E fields. The validation [15] is divided into the following four steps.

- 1) Develop validation trajectories in the phantom containing tissue simulating media.
- 2) Measure the lead-tip temperature rise for each validation trajectory developed in step 1.
- 3) Compute the lead-tip temperature rise using the TF for each validation trajectory developed in step 1.
- 4) Compute the error between the measured and computed temperature rise, if it is less than the combined uncertainty, i.e., the experimental and the computational uncertainty, the TF can be considered validated.

B. Design Method for Optimized Validation Trajectories

Step 1 is critical for the TF validation because poorly designed trajectories result in inadequately validated TFs. Ideally, the E-field distribution along the validation trajectories should be linearly independent (which would be ideal), or at least have a low correlation to each other, and results in a high lead-tip temperature rise [20], [21] to increase the SNR. To develop such a set of optimized trajectories we randomly select a trajectory on the circular plate, rotate the plate several times, and optimize the trajectory using PSO, as described in [27].

First, we segment the randomly selected fixed trajectory in N straight segments so that each segment is $L_N = L/N$ long. A trajectory can then be uniquely defined by its starting point P_1 and the N angles $\vec{\theta} = (\theta_1, \, \theta_2, \ldots, \theta_N)$ for each segment, where $\theta_n = \arg(\vec{P}_{n+1} - \vec{P}_n)$. With $\vec{P}_1(P_{1x}, \, P_{1y})$ the starting point of the trajectory and $(0, \, 0)$ the center of the circular plate, the first trajectory can be calculated using

$$P_{(n+1)x} = P_{nx} + L_N \cdot \cos(\theta_n)$$

$$P_{(n+1)y} = P_{ny} + L_N \cdot \sin(\theta_n)$$

$$\vec{P}_n = (P_{nx}, P_{ny})$$

$$1 \le n \le N$$
(3)

However, there are two constraints to satisfy. The first one is that all segments L_N must be located on the circular plate. For a plate with a radius R_P , the first constraint can be defined as Constraint $1: \sqrt{P_{nx}^{\ \ 2} + P_{ny}^{\ \ 2}} \leq R_P$. The second constraint limits the bending angle θ_n between two segments. The bending angle must be larger than 90° , which leads to Constraint $2: |\theta_{n+1} - \theta_n| < 90^\circ$. Constraint 2 is due to the mechanical limitations of the lead, which should not be bent sharply. The first trajectory is calculated by assigning random values to the N angles θ_n while satisfying the two constraints.

Then, the first trajectory is rotated R times with a degree of Φ_R , resulting in R+1 trajectories. Next, E_{tan} for each trajectory (length L) is sampled S times, resulting in $L_S = L/S$ E-field values. These $E_{\rm tan}$ values are arranged in a $(R+1) \times L_S$ matrix, where each row of $\mathbb{E}_{\mathrm{tan}}$ represents the tangential E-field of a particular trajectory. $\mathbb{E}_{\mathrm{tan}}$ can then be decomposed in $\mathbb{E}_{tan} = \mathbb{U} \cdot \Sigma \cdot \mathbb{V}^T$ according to the singular value decomposition [25]. It is convenient to use the following notation for the singular values: $\lambda_j(\mathbb{E}_{ an})$ is the jth largest singular value of \mathbb{E}_{\tan} with $j = 1, 2, 3, ..., \min \{(R+1), L_S\}; \lambda_{\max}(\mathbb{E}_{\tan})$ is the largest singular value; and $\lambda_{\min}(\mathbb{E}_{\tan})$ the smallest singular value of \mathbb{E}_{tan} . The condition number k of \mathbb{E}_{tan} is defined as $k = \lambda_{\max}(\mathbb{E}_{\tan})/\lambda_{\min}(\mathbb{E}_{\tan})$, which is also called the cost function of the PSO algorithm. The cost function k depends on the PSO particle θ_i , i.e., $k(\theta_i)$. The lower k is, the less E_{tan} along the R+1 trajectories are correlated to each other.

Finally, we minimize the cost function $k(\vec{\theta}_i)$ using PSO. The workflow of the PSO is illustrated as follows. The vector $\vec{\theta}$ is called a particle of the PSO algorithm. The number of particles is I, with $\vec{\theta}_i$ the ith particle. The PSO iteration loop is executed until the maximum number of iterations T or the minimum error criteria err_0 is reached. The error is defined as

err = $|k_t(\vec{\theta}_i) - k_{t-1}(\vec{\theta}_i)| < \text{err}_0$, where $k_t(\vec{\theta}_i)$ and $k_{t-1}(\vec{\theta}_i)$ are the cost functions of tth and (t-1)th iteration, respectively. In each iteration t the particle velocity $\vec{\theta}_{vi}$ and the particle $\vec{\theta}_i$ are updated using

$$\vec{\theta}_{v(i+1)} = w \cdot \vec{\theta}_{vi} + c_1 \cdot \text{Rand} \cdot \left(\vec{\theta}_{BLi} - \vec{\theta}_i\right) + c_2 \cdot \text{Rand} \cdot \left(\vec{\theta}_{BG} - \vec{\theta}_i\right)$$
(4)

$$\vec{\theta}_{i+1} = \vec{\theta}_i + \vec{\theta}_{v(i+1)} \tag{5}$$

where w is a constant called the inertia weight, c_1 and c_2 are two coefficients, which are chosen according to Liu et al. [26], and $\vec{\theta}_{\mathrm{BL}i}$ and $\vec{\theta}_{\mathrm{BG}}$ are the best-local (BL) position for the ith particle and best-global (BG) position (the final result of the PSO), respectively. Each BL position $\vec{\theta}_{\mathrm{BL}i}$ is initialized with the first particle $\vec{\theta}_i$ and the BG position $\vec{\theta}_{\mathrm{BG}}$ is initialized with the BL position, which minimizes the cost function $k(\vec{\theta}_{\mathrm{BL}i})$. Rand is a random number generated by a random number generator. The trajectory generation algorithm using PSO described in [27] can be summarized as follows.

```
CALCULATE FIRST TRAJECTORY
      Calculate \vec{P}_1 to \vec{P}_N by randomly
selecting \vec{\theta}_i.
While particle ec{	heta}_i satisfies Constraint 1
and 2
DEFINE COST FUNCTION
Rotate the first trajectory R times.
Sample E_{\mathrm{tan}} for each trajectory S times.
Establish \mathbb{E}_{\mathrm{tan}} matrix and calculate
condition number k.
Define I random particles \vec{\theta_i}.
Calculate cost function k(\vec{\theta_i}) for each
particle \vec{\theta_i}.
 \vec{\theta}_{\mathrm{BL}i} = \vec{\theta}_i \, .  Set \vec{\theta}_{\mathrm{BG}} = \vec{\theta}_{\mathrm{BL}i}, which minimizes k(\vec{\theta}_{\mathrm{BL}i}) \, . 
MINIMIZE CONDITION NUMBER OF \mathbb{E}_{\mathrm{tan}} USING
PSO
Do {
      Calculate k(\vec{\theta_i}).
      If k(ec{	heta}_i) is less than k(ec{	heta}_{\mathrm{BL}i}) and PP
ec{	heta}_i satisfies _Constraints 1 and 2 set BL
position to ec{	heta}_{\mathrm{BL}i} = ec{	heta}_i .
      Choose the smallest k(\vec{	heta}_{\mathrm{BL}i}) and set
BG position ec{	heta}_{
m BG}=ec{	heta}_{
m BL}{}_i . Update particle velocity ec{	heta}_{v(i+1)} using
      Update particle \vec{\theta}_{i+1} using (5).
While maximum iterations or minimum
error criteria are not met.
```

Applying the proposed algorithm, R+1 optimized validation trajectories for any lead length can be generated.

C. Effect of the Circular Plate on the E-Field Distribution

The lead validation trajectories are implemented on a rotatable circular plate, as shown in Fig. 1. The rotatable circular plate consists of three parts. The first part is the top beam with a plastic bearing. A wood stick and protractor mounted on the top beam are used to measure the rotation angle of the plate. The second part is the circular plate made out of an acrylic grid. Serving as the backbone, the third part connects the top beam and the circular plate. The entire structure is made of acrylic material, which is nonmagnetic and nonmetallic, and thus MRIcompatible with little influence on the E-field. The AIMD with lead and temperature probes are fixed on the plate, which is positioned 10 cm in the x-direction and 15 cm in the z-direction from the center of the rectangular phantom. The E-field in this region is much higher than that in the center of the phantom, which leads to a better SNR. The entire setup is then exposed to the fields of the RF coil. When the plate rotates by a specific angle, the incident E-field along the lead trajectories changes.

D. Validation Strategy

The experimental validation strategy is divided into the following three steps.

- The TF measurement using the method mentioned in Section II.
- 2) The radiated test in the RF coil: The AIMD and lead are placed according to the precalculated rotation trajectories, and the lead-tip temperature rises are measured for all trajectories. If the SNR of one or more trajectories is low, extra rotation trajectories and heating measurements can be added until the SNR of all trajectories is acceptable. By repeating the previous procedure without AIMD and leads, a set of nine background temperature rises can be recorded. The net temperature rise equals the measured lead-tip temperature rise minus the corresponding background temperature rise at that location.
- 3) The computational lead-tip heating prediction: The incident E-field along the rotation-invariant trajectories is extracted from numerical simulations. Then the TF is used to predict the lead-tip temperature rise for each trajectory using (2).

The TF is validated if the total error between the measured and computed lead-tip heating is less than the combined uncertainty.

III. RESULTS

A. Electromagnetic Simulations of the Circular Plate

To numerically simulate the incident E-field distribution in the phantom with the circular plate, a three-dimensional model is built in SEMCAD X, as shown in Fig. 2(b). A standard high-pass birdcage RF coil with a diameter of 63 cm and a length of 65 cm was developed to simulate the incident E-field. The rectangular phantom with the circular plate is positioned at the isocenter of the RF coil. The acrylic material has a relative permittivity

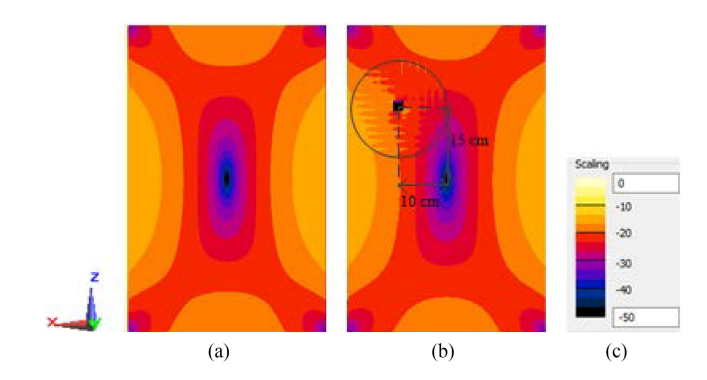


Fig. 2. (a) Incident E-field (rms) in the central planes along the axial direction without the plate present. (b) With the plate present. (c) Scaling of both figures (dB).

of 3.5. The phantom material, i.e., gelled saline, has a depth of 9 cm, an electric conductivity of 0.47 S/m, and a relative dielectric permittivity of 78, respectively. This phantom material is equivalent to the high-permittivity medium recommended in ISO/TS 10974 [15]. The upper surface of the circular plate is 4.5 cm below the surface of the gel. Fig. 2(a)–(c) shows the E-field distributions for the linear polarization of the RF coil in the central plane along the axial direction with, and without, the plate in place. As can be seen in Fig. 2(b), the overall E-field distribution is not changed significantly, only minor perturbations occur.

B. Development of Optimized Validation Trajectories

Based on the methodology described in Section II-B, nine trajectories for leads from 15 to 50 cm were developed. The trajectory segment length L_N is 5 cm and the trajectory rotation angle Φ_R is 45°. The circular plate radius R_P is 10 cm and the starting point P_1 is located at [9, 0] cm, with the center of the plate [0, 0]. The maximum PSO iteration is 200 and the population of particles is 20. w, c_1 , and c_2 are chosen to be 0.73, 1.50, and 1.50, respectively. The minimum error criterion err_0 is 0.01. Changes in all of these parameters did not significantly alter the PSO outcome, i.e., the condition number of \mathbb{E}_{tan} . The RF coil is driven in a linear mode and the trajectory for each lead is rotated eight times, generating nine validation trajectories. The sampling size of the E-field along the trajectory is 1 cm. For example, for a lead length of 30 cm, $\mathbb{E}_{\mathrm{tan}}$ will be a 9 \times 30 complex matrix. The optimized trajectories for leads' lengths of 15–50 cm are illustrated in Fig. 3.

To compare our optimized trajectories with the SLU trajectories (as used in [14]) and the trajectories proposed by ISO/TS 10974, we calculate the E-field along these two sets of trajectories. From these E fields, we generate two complex \mathbb{E}_{tan} matrices, $\mathbb{E}_{\text{tan}, \text{SLU}}$ and $\mathbb{E}_{\text{tan}, \text{ISO}}$, and calculate their condition number k_{SLU} and k_{ISO} . The five ISO/TS 10974 trajectories are shown in Fig. 4. To generate also nine validation trajectories we extracted the tangential E-field for four of the five ISO/TS 10974 trajectories for both linear and circular polarizations as well as the fifth ISO/TS 10974 trajectory only for the linear polarization. So $\mathbb{E}_{\text{tan}, \text{ISO}}$ would also be a $(2 \times 4 + 1 = 9)$ -column matrix.

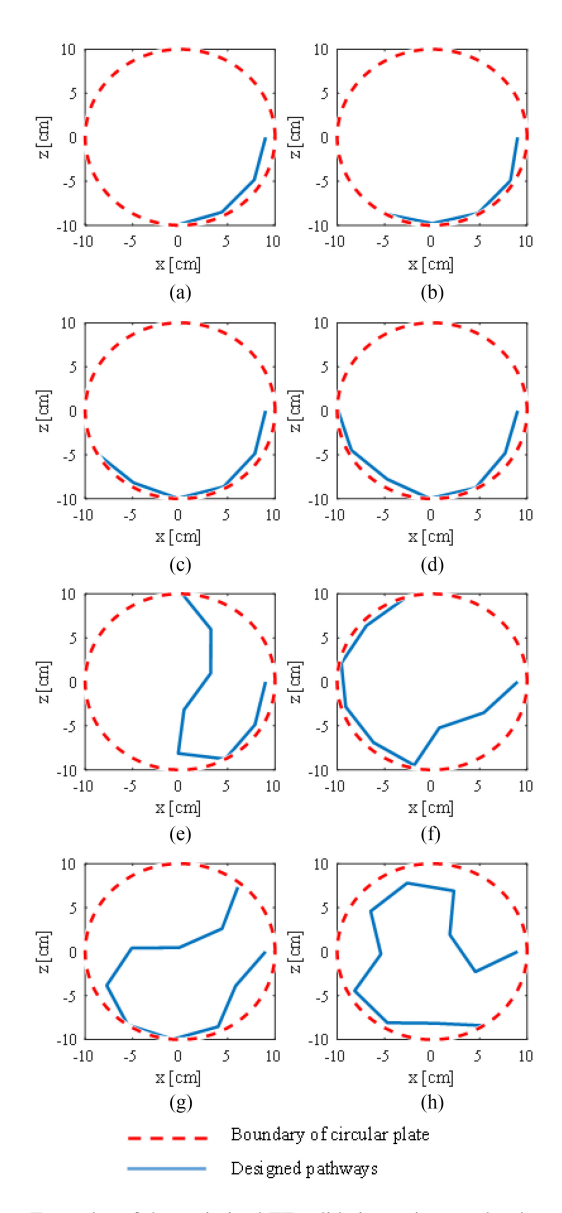


Fig. 3. Examples of the optimized TF validation trajectory developed using the PSO algorithm for different AIMD lead lengths L: (a) 15 cm; (b) 20 cm; (c) 25 cm; (d) 30 cm; (e) 35 cm; (f) 40 cm; (g) 45 cm; (h) 50 cm.

For the ISO/TS 10974 trajectory in Fig. 4(a), each of the three segments has a length of L/3. For the trajectory in Fig. 4(b), we extracted the E-field along the trajectory starting from P1. The trajectory in Fig. 4(c) is designed for different lengths as a circle with $r=\frac{L}{2\pi}$. The fourth and fifth trajectory in Fig. 4(d) and (e) is selected from the phase reversal point, i.e., P2 and P3 in the figure, toward the end of the trajectories. The length of each segment separated by the phase reversal point is L/2. With this trajectory selection method, the phase reversal, amplitude ramp, and phase ramp in the ISO/TS 10974 trajectories have been fully considered to ensure a fair comparison with our optimized trajectories. The trajectories used in [14] are illustrated in Fig. 5. The L-shape trajectory has two segments with lengths of L-8 cm and 8 cm, respectively, while the U-shape trajectory has three segments with lengths of (L-8 cm)/2, 8 cm, and (L-8 cm)/2,

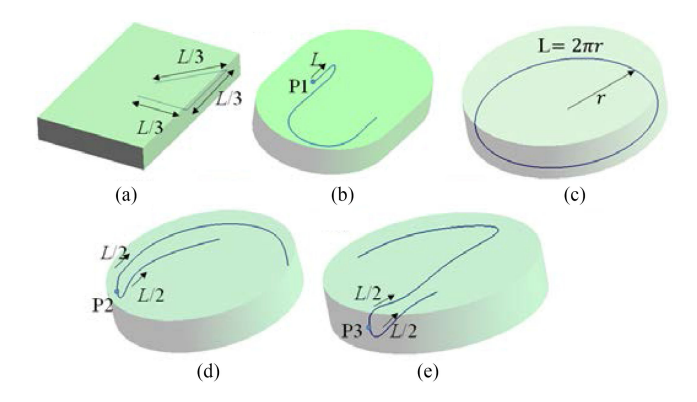


Fig. 4. ISO/TS 10974, Annex M recommended TF validation trajectories. (a) Trajectory in the rectangular phantom. (b) Trajectory in the oval phantom. (c), (d), (e) Trajectories in the circular phantom.

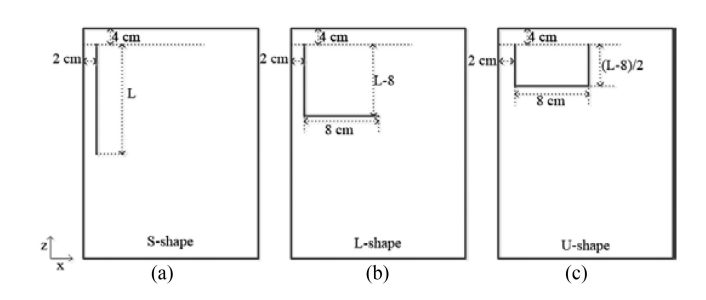


Fig. 5. Validation trajectories used in [14]. (a) S-shape trajectory. (b) L-shape trajectory. (c) U-shape trajectory. Each of these three trajectories is shifted 4 and 8 cm in the x-direction, so a total of nine trajectories were used for the $\mathbb{E}_{\tan, \, \mathrm{SLU}}$ matrix.

TABLE I COMPARISON OF THE CONDITION NUMBER FOR THE $\mathbb{E}_{\mathrm{tan,\ ISO}}$ AND $\mathbb{E}_{\mathrm{tan,\ SLU}}$ MATRIX WITH THE CONDITION NUMBER OF OUR NOVEL OPTIMIZED TRAJECTORIES GENERATED USING THE PSO ALGORITHM

Lead length [cm]	ISO/TS 10974 Trajectories	SLU Trajectories	PSO Optimized Trajectories
	k_{ISO}	k_{SLU}	k
15	58782	17390	13377
20	32108	9380	5789
25	37472	8024	1653
30	36650	6067	1132
35	21561	6372	2253
40	28810	6161	952
45	28810	7540	912
50	31628	7721	983

respectively. Each of three trajectories is shifted for 4 and 8 cm in the *x*-direction, so $\mathbb{E}_{\mathrm{tan,\ SLU}}$ would be also a (3 \times 3 = 9)-column matrix. The E-field along these trajectories in Figs. 4 and 5 is extracted and the condition number is given in Table I.

As illustrated in Table I, the condition numbers of our PSO optimized rotation-invariant trajectories are much lower than the ISO/TS 10974 or SLU trajectories, even for short leads. The E fields along these optimized trajectories are, therefore, less correlated and thereby improving the validation performance.

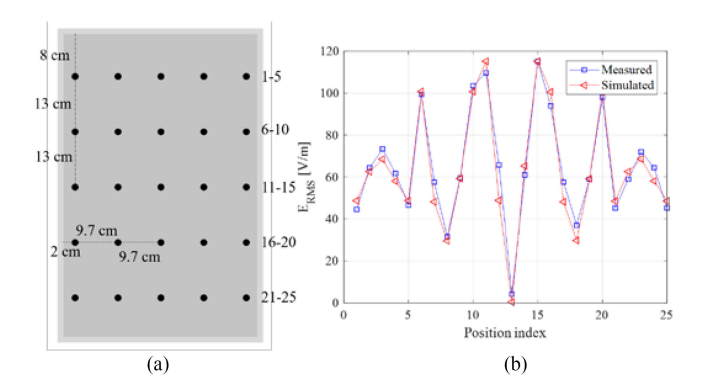


Fig. 6. (a) E-field validation positions in the rectangular phantom. (b) Measured and simulated E-field (rms value) inside the rectangular phantom exposed to the MITS 1.5 T coil in a linear polarization at 2 W/kg.

C. Experimental Validation

To experimentally confirm the feasibility of the proposed PSO trajectory optimization method, we use two commercial AIMDs and validate their TFs. The medical implant test system MITS 1.5 (Zurich MedTech ZMT, Zurich, Switzerland) was used to mimic the exposure of the AIMDs in 1.5 T (64 MHz) MRI scanners. The RF coil is driven in a linear polarization at 2 W/kg whole-body average SAR. The measured and simulated E-field distribution in the rectangular phantom was compared at 25 points, as shown in Fig. 6, showing good agreement with an average relative error of 3.5%. The lead-tip temperature rise after a 2 min exposure was measured using the Neoptix optical temperature probes manufactured by Qualitrol Corp. [30].

The mounting of two commercial AIMDs on the circular plate is illustrated in Fig. 7(a) and (b) showing the temperature probe placed next to the lead tip. The circular plate inside the rectangular phantom in the MITS 1.5 T RF coil is shown in Fig. 7(d).

Two commercial AIMDs with a helical wire structure are selected. AIMD 1 is a spinal cord stimulator with a lead length of 30 cm and AIMD 2 is a sleep apnea stimulator with a lead length of 45 cm. The PSO optimized validation trajectory for the 30 cm and the 45 cm lead is shown in Fig. 3(d) and (g), respectively. The TF for both leads was measured and validated using nine optimized trajectories. To guarantee sufficient SNR, additional trajectories were computed and used for the validation if the lead-tip temperature rise was less than 2 °C. For accurate validation results, it is important that the gel temperature is the same before each lead-tip measurement; if necessary, a stirring rod can be used to equalize the gel temperature. The TF for both AIMD leads is shown in Fig. 8(a) and (b). Fig. 8(c) and (d) shows the measured and computed net (temperature rise minus background heating) lead-tip heating. To achieve sufficient SNR, the exposure level of whole-body average SAR was changed to 3 W/kg in the validation experiment and verified using the calorimetry method [28]. The good validation results with deviations less than 2σ prove the feasibility of the proposed PSO validation trajectory development method.

The uncertainty was assessed following technical report TR21900 [29]. The detailed uncertainty sources and their

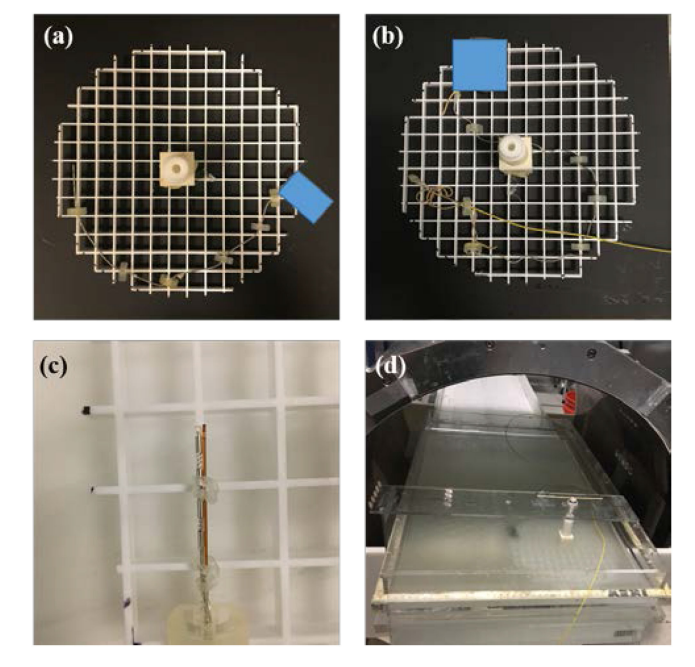


Fig. 7. Fixing of the AIMDs on the circular plate. (a) AIMD 1 with a 30 cm lead. (b) AIMD 2 with a 45 cm lead. The blue rectangles covering the implantable pulse generators are used to avoid the disclosure of commercial information. (c) Close-up view of the temperature probe position. (d) Circular plate inside the rectangular phantom in the MITS 1.5 T RF coil.

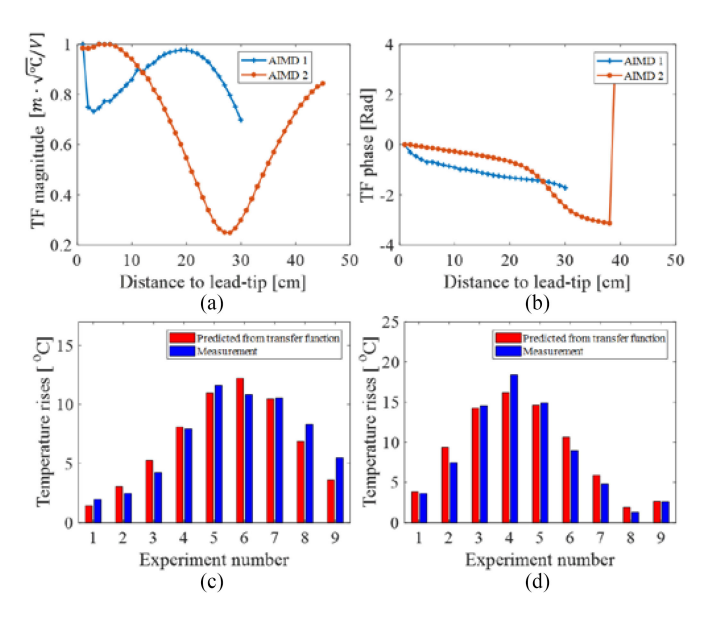


Fig. 8. (a) TF magnitude of two AIMDs. (b) TF phase of two AIMDs. (c) Validation results for AIMD 1. (d) Validation results for AIMD 2.

individual uncertainties, as well as the combined uncertainty for the validation test, are given in Table II. The combined plot of the TF predicted and measured lead-tip heating, including uncertainty, is shown in Fig. 9.

Our novel PSO validation trajectory method is also applicable for AIMDs with multiple leads or multiple electrodes. For AIMDs with multiple leads, e.g., an AIMD with two 40 cm leads, one can use the PSO algorithm to generate two sets

TABLE II					
VALIDATION UNCERTAINTY BUDGET					

Computational Un	certainty	Experimental Uncertainty	
Source of Uncertainty	[%]	Source of Uncertainty	[%]
Grid resolution	1.2	B1 _{RMS}	4.1
Liquid conductivity	6.6	Drift of B1 _{RMS}	2.3
and permittivity		Drift of E _{RMS}	3.2
Lead path	9.2	Phantom position	0.2
Dielectric mesh	4.4	Coil length	3.5
Dicicetite mesii		Coil diameter	7.1
Temperature readout [30]		± 0.2°C	
Combined uncertainty		15.6± 0.2°C	

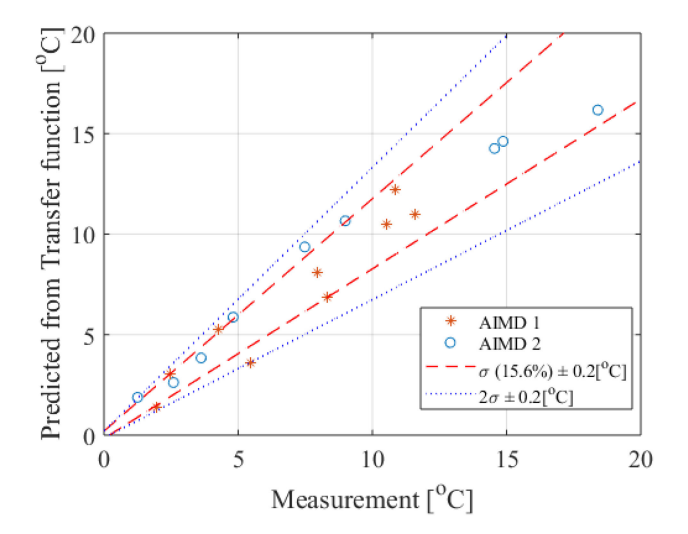


Fig. 9. Comparison of calculated and measured lead-tip heating for AIMDs 1 and 2.

of 40 cm validation trajectories, one for each lead but with the same starting point for the implantable pulse generator. For the measurements, two thermal probes are needed to measure the heating for each lead tip. For AIMDs with multiple electrodes but single lead, one can still use the trajectories shown in Fig. 3 with extra thermal probes for the multiple electrodes.

IV. CONCLUSION

This article presents a novel PSO-based algorithm to generate optimized transfer function validation trajectories for AIMDs with different lead lengths. The E-fields along the optimized trajectories are much less correlated than those recommended by ISO/TS 10974 or other literature, e.g., [14], leading to a significantly improved validation. The new validation strategy requires only a single phantom, single excitation mode, and no repositioning of the leads, making it significantly more robust, effective, accurate, and time efficient; and therefore an ideal candidate for standardization.

Disclaimer: The mention of commercial products, their sources, or their use in connection with material reported herein is not to be construed as either an actual or suggested endorsement of such products by the Department of Health and Human Services.

REFERENCES

- [1] J. A. Nyenhuis, A. V. Kildishev, J. D. Bourland, K. S. Foster, T. W. Athey, and G. Graber, "Heating near implanted medical devices by the MRI RF-magnetic field," *IEEE Trans. Magn.*, vol. 35, no. 5, pp. 4133–4135, Sep. 1999.
- [2] U. D. Nguyen, J. S. Brown, I. A. Chang, J. Krycia, and M. S. Mirotznik, "Numerical evaluation of heating of the human head due to magnetic resonance imaging," *IEEE Trans. Biomed. Eng.*, vol. 51, no. 8, pp. 1301–1309, Aug. 2004.
- [3] A. Amjad, R. Kamondetdacha, A. V. Kildishev, S. M. Park, and J. A. Nyenhuis, "Power deposition inside a phantom for testing of MRI heating," *IEEE Trans. Magn.*, vol. 41, no. 10, pp. 4185–4187, Oct. 2005.
- [4] J. A. Nyenhuis, S.-M. Park, R. Kamondetdacha, A. Amjad, F. G. Shellock, and A. R. Rezai, "MRI and implanted medical devices: Basic interactions with an emphasis on heating," *IEEE Trans. Device Mater. Rel.*, vol. 5, no. 3, pp. 467–480, Sep. 2005.
- [5] R. Guo et al., "Computational and experimental investigation of RF-induced heating for multiple orthopedic implants," Magn. Reson. Med., vol. 82, no. 5, pp. 1848–1858, 2019.
- [6] Y. Wang et al., "A novel device model validation strategy for 1.5- and 3-T MRI heating safety assessment," *IEEE Trans. Instrum. Meas.*, vol. 69, no. 9, pp. 6381–6389, Sep. 2020.
- [7] P. Nordbeck et al., "Measuring RF-induced currents inside implants: Impact of device configuration on MRI safety of cardiac pacemaker leads," Magn. Reson. Med., vol. 61, no. 3, pp. 570–578, 2009.
- [8] L. M. Angelone, J. Ahveninen, J. W. Belliveau, and G. Bonmassar, "Analysis of the role of lead resistivity in specific absorption rate for deep brain stimulator leads at 3T MRI," *IEEE Trans. Med. Imag.*, vol. 29, no. 4, pp. 1029–1038, Apr. 2010.
- [9] E. Mattei et al., "Complexity of MRI induced heating on metallic leads: Experimental measurements of 374 configurations," *Biomed. Eng. Online*, vol. 7, 2008, Art. no. 11.
- [10] E. Zastrow, E. Cabot, and N. Kuster, "Assessment of local RF-induced heating of AIMDs during MR exposure," in *Proc. 31st Gen. Assem. Sci. Symp. Int. Union Radio Sci.*, Beijing, China, Aug. 2014, pp. 1–4, doi: 10.1109/URSIGASS.2014.6930111.
- [11] Y. Wang *et al.*, "On the development of equivalent medium for active implantable device radiofrequency safety assessment," *Magn. Reson. Med.*, vol. 82, no. 3, pp. 1164–1176, 2019.
- [12] E. Cabot, E. Zastrow, and N. Kuster, "Safety assessment of AIMDs under MRI exposure: Tier3 vs. Tier4 evaluation of local RF-induced heating," in *Proc. Int. Symp. Electromagn. Compat.*, Tokyo, Japan, May 12–16, 2014, pp. 237–240.
- [13] S.-M. Park, R. Kamondetdacha, and J. A. Nyenhuis, "Calculation of MRI-induced heating of an implanted medical lead wire with an electric field transfer function," *J. Magn. Reson. Imag.*, vol. 26, no. 5, pp. 1278–1285, 2007.
- [14] S. Feng, R. Qiang, W. Kainz, and J. Chen, "A technique to evaluate MRI-induced electric fields at the ends of practical implanted lead," *IEEE Trans. Microw. Theory Techn.*, vol. 63, no. 1, pp. 305–313, Jan. 2015.
- [15] Assessment of the Safety of Magnetic Resonance Imaging for Patients With an Active Implantable Medical Device, ISO/TS Standard 10974:2018, Apr. 2018.
- [16] M. Kozlov and W. Kainz, "Comparison of different assessment quantities to evaluate lead electromagnetic model for radio frequency energy-induced heating," *IEEE J. Electromagn. RF Microw. Med. Biol.*, vol. 4, no. 3, pp. 157–163, Sep. 2020.
- [17] E. Zastrow, A. Yao, and N. Kuster, "Practical considerations in experimental evaluations of RF-induced heating of leaded implants," in *Proc. 32nd Gen. Assem. Sci. Symp. Int. Union Radio Sci.*, Montreal, QC, Canada, Aug. 19–26, 2017, pp. 1–4, doi: 10.23919/URSIGASS.2017.8105350.
- [18] A. Yao, E. Zastrow, E. Neufeld, M. Cabanes-Sempere, T. Samaras, and N. Kuster, "Novel test field diversity method for demonstrating magnetic resonance imaging safety of active implantable medical devices," *Phys. Med. Biol.*, vol. 65, 2020, Art. no. 075004.

- [19] M. Kozlov, M. Horner, and W. Kainz, "Modeling radiofrequency responses of realistic multi-electrode leads containing helical and straight wires," Magn. Reson. Mater. Phys., Biol. Med., vol. 33, pp. 421-437, 2020.
- [20] Z. Wang, J. Zheng, Y. Wang, W. Kainz, and J. Chen, "On the model validation of active implantable medical device for MRI safety assessment," IEEE Trans. Microw. Theory Techn., vol. 68, no. 6, pp. 2234-2242, Jun. 2020.
- [21] I. Weiss and T. Aimd, "Path assessment for AIMD model validation," in Proc. Notes ISO/TS 10974 Annex M Subgroup Meeting, 2013.
- [22] E. Neufeld, S. Kühn, G. Szekely, and N. Kuster, "Measurement, simulation and uncertainty assessment of implant heating during MRI," Phys. Med. Biol., vol. 54, pp. 4151-4169, 2009.
- Y. Wang, J. Zheng, Q. Wang, and J. Chen, "A fast and accurate transfer function validation strategy using rotational invariant lead trajectories," in Proc. IEEE Int. Symp. Antenna Propag., Jul. 7-12, 2019, pp. 357-358.
- [24] L. Yan, Q. Shen, H. Lu, H. Wang, X. Fu, and J. Chen, "Inversion and uncertainty assessment of ultra-deep azimuthal resistivity logging-while-drilling measurements using particle swarm optimization," J. Appl. Geophys., vol. 178, Jul. 2020, Art. no. 104059.
- [25] G. H. Golub and C. Reinsch, "Singular value decomposition and least squares solutions," Numer. Math., vol. 14, no. 5, pp. 403-420, 1970.
- [26] S. Liu, M. Liang, and X. Hu, "Particle swarm optimization inversion of magnetic data: Field examples from iron ore deposits in China," Geophysics, vol. 83, no. 4, pp. J43-J59, Jul. 2018.
- [27] X. Hu and R. Eberhart, "Solving constrained nonlinear optimization problems with particle swarm optimization," in Proc. 6th World Multiconf. Syst. Cybern. Inform., Orlando, FL, USA, Jul. 14–18, 2002, pp. 203–206.
- Standard Test Method for Measurement of Radio Frequency Induced Heating on or Near Passive Implants During Magnetic Resonance Imaging, ASTM Standard F2182, Apr. 2020.
- [29] Guidance for Uncertainty Analysis Regarding the Application of ISO/TS 10974, ISO/TR Standard 21900:2018, Sep. 2018.
- "Field proven fiber optic temperature sensors," T1 Fiber Opt. Temp. Probe, Neoptix, Québec City, QC, Canada, 2017. [Online]. Available: https:// www.neoptix.com/t1-sensor.asp, Accessed: Feb. 3, 2020.



RF measurement.

Qingyan Wang received the B.S. degree in electronics and information engineering from the Huazhong University of Science and Technology, Wuhan, China, in 2011, and the Ph.D. degree in electrical engineering from the University of Houston, Houston, TX, USA, in 2016.

Since 2016, he has been a Postdoctoral Researcher with the University of Houston, Houston, TX. His current research interests include applied electromagnetics on biomedical applications, magnetic resonance imaging radio frequency (RF) safety modeling, and

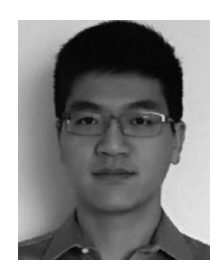


Ji Chen (Senior Member, IEEE) received the B.S. degree from the Huazhong University of Science and Technology, Wuhan, China, in 1989, the M.S. degree from McMaster University, Hamilton, ON, Canada, in 1994, and the Ph.D. degree from the University of Illinois, Champaign, IL, USA, in 1998, all in electrical

He is currently a Professor with the Department of Electrical Engineering, University of Houston, Houston, TX, USA. His research interests include microprocessor full chip-level interconnect extrac-

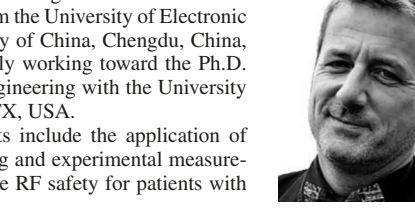
tion, wireless communication system-on-chip interconnect characterization, computer system electromagnetic compatibility/electromagnetic interference modeling, signal integrity analysis, and bioelectromagnetics with applications to MRI systems.

Prof. Chen was a recipient of the ORISE Fellowship in 2006 and the Motorola Engineering Award in 2000.



Yu Wang received the B.S. degree in electronic information engineering from the University of Electronic Science and Technology of China, Chengdu, China, in 2016, and is currently working toward the Ph.D. degree in electronic engineering with the University of Houston, Houston, TX, USA.

His research interests include the application of computational modeling and experimental measurements aimed to evaluate RF safety for patients with medical implants.





Jianfeng Zheng (Member, IEEE) received the B.S. degree in electronic information engineering and the Ph.D. degree in electronic science and technology from Tsinghua University, Beijing, China, in 2002 and 2009, respectively.

He was an Assistant Researcher with the State Key Laboratory on Microwave and Digital Communications, Tsinghua University. Since 2012, he has been a Postdoctoral Fellow with the Department of Electrical and Computer Engineering, University of Houston, Houston, TX, USA. His current research interests

include applied electromagnetics on biomedical applications, MRI RF safety, multiple-input multiple-output channel measurements, and antenna arrays for MIMO communications.



Wolfgang Kainz (Member, IEEE) received the Ph.D. degree in technical science from the Vienna University of Technology, Vienna, Austria, in 2000.

After working for the Austrian Research Center Seibersdorf, he joined the Foundation for Research on Information Technologies in Society (IT'IS), Zurich, Switzerland, as an Associate Director. At IT'IS, he worked on the development of in vivo and in vitro exposure setups for bioexperiments. Since 2002, he has been a Research Biomedical Engineer with the Center for Devices and Radiological Health, Food and

Drug Administration, Silver Spring, MD, USA. He has authored or coauthored more than 200 peer-reviewed articles and book chapters. In 2004, he initiated the Virtual Family Project in cooperation with IT'IS and Prof. J. Chen from the University of Houston. In 2016, he initiated o2S2PARC (Open Online Simulations for Stimulating Peripheral Activity to Relieve Conditions, https://osparc.io/) in cooperation with IT'IS. His research interest is focused on the safety and effectiveness of medical devices and the safety of humans in electromagnetic fields. This includes novel computational life science methods for safety and effectiveness evaluations using the functionalized anatomical models of the human anatomy; magnetic resonance imaging (MRI) safety; performance and safety of wireless technology used in medical devices; electromagnetic compatibility of medical devices; dosimetric exposure assessments from dc to light; and novel methods to computationally assess the safety and effectiveness of new neuroprosthetics, e.g., electroceuticals, and therapeutic stimulation methods.

Dr. Kainz was a recipient of the prestigious FDA Award of Merit in 2010 for exceptional leadership in performance in addressing the issues of compatibility of medical devices during MRI by applying transparently scientific research to device regulation. He is a Senior Member of the Administrative Committee of the IEEE International Committee on Electromagnetic Safety and a Member of many International Standards Committees.